JGR Oceans

RESEARCH ARTICLE
10.1029/2020JC016544

Key Points:
- Ocean heat flux is large at high frequency
- Such high-frequency flux is generated at submesoscale
- Such heat flux is a key component of global heat budget

Supporting Information:
- Supporting Information S1

Correspondence to:
Z. Su,
zhansu@physics.utoronto.ca

Citation:
Su, Z., Torres, H., Klein, P., Thompson, A. F., Siegelman, L., Wang, J., et al. (2020). High-frequency submesoscale motions enhance the upward vertical heat transport in the global ocean. *Journal of Geophysical Research: Oceans*, *125*, e2020JC016544. https://doi.org/10.1029/2020JC016544

Received 26 JUN 2020
Accepted 13 AUG 2020
Accepted article online 18 AUG 2020

High-Frequency Submesoscale Motions Enhance the Upward Vertical Heat Transport in the Global Ocean

Zhan Su[1], Hector Torres[2], Patrice Klein[2,3], Andrew F. Thompson[4], Lia Siegelman[2], Jinbo Wang[2], Dimitris Menemenlis[2], and Christopher Hill[5]

[1]Department of Physics, University of Toronto, Toronto, ON, Canada, [2]Jet Propulsion Laboratory, California Institute of Technology, Pasadena, CA, USA, [3]IFREMER, CNRS, Paris, France, [4]Environmental Science and Engineering, California Institute of Technology, Pasadena, CA, USA, [5]Department of Earth, Atmospheric and Planetary Sciences, Massachusetts Institute of Technology, Cambridge, Massachusetts, USA

Abstract The rate of ocean heat uptake depends on the mechanisms that transport heat between the surface and the ocean interior. A recent study found that the vertical heat transport driven by motions with scales smaller than 0.5° (submesoscales) and frequencies smaller than 1 day^{-1} is upward. This transport competes with the other major components of the global heat transport, namely, the downward heat transport explained by the large-scale wind-driven vertical circulation and vertical diffusion at small scales and the upward heat transport associated with mesoscale eddies (50- to 300-km size). The contribution from motions with small spatial scales (<0.5°) and frequencies larger than 1 day^{-1}, including internal gravity waves, has never been explicitly estimated. This study investigates this high-frequency (subdaily) submesoscale contribution to the global heat transport. The major result of this study, based on the analysis of a high-resolution ocean model, is that including this high-frequency contribution surprisingly doubles the upward heat transport due to submesoscales in winter in the global ocean. This contribution typically concerns depths down to 200–500 m and can have a magnitude of up to 500 W m^{-2} in terms of wintertime heat fluxes at 40-m depth, which causes a significant upward heat transport of ~7 PW when integrated over the global ocean. Thus, such submesoscale heat transport, which is not resolved by climate models, impacts the heat uptake in the global ocean. The mechanisms involved in these results still need to be understood, which should be the scope of future work.

1. Introduction

Transient climate change can be defined in terms of surface air temperature change and thus is fundamentally linked to the mechanisms that vertically transport heat from the air-sea interface down to the ocean interior, which contribute to setting the rate of ocean heat uptake (Griffies et al., 2015). Oceanic motions that govern these mechanisms cover a broad range of spatial and temporal scales, from centimeters to kilometers and from minutes to decades (Ferrari & Wunsch, 2009; Klein & Lapeyre, 2009). In the past 10 years, there has been a growing appreciation for the role of ocean mesoscale eddies (with typical spatial scales of 50–300 km, temporal scales of days to months and therefore with small Rossby number) for the vertical heat transport. These eddies, which account for most of the kinetic energy in the global ocean (Ferrari & Wunsch, 2009), are now thought to explain most of the upward vertical heat transport leading to warm the upper oceanic layers and cool lower layers (Wolfe et al., 2008). This transport is balanced by the downward heat transport explained by the large-scale wind-driven vertical circulation as well as small-scale diffusive processes (that include small-scale processes not explicitly resolved by climate models) (Griffies et al., 2015).

Numerical studies of the past 5 to 10 years (see Fox-Kemper et al., 2011; Griffies et al., 2015) have pointed to another contribution to the vertical heat transport. This contribution involves motions with scales smaller than 0.5° (~50 km in midlatitudes), called submesoscales in this study (see McWilliams, 2016, for a review). Submesoscale motions include those associated with submesoscale thermal fronts and mixed-layer instabilities (MLIs) that are principally driven by the strain field of mesoscale eddies (Callies et al., 2016; Capet et al., 2008a; Fox-Kemper et al., 2008; Ferrari, 2011; Lapeyre et al., 2006). They are characterized by large

Rossby number and small Richardson number, and, as such, they are balanced motions in gradient wind balance (i.e., with the nonlinear terms having the same order of magnitude as the Coriolis term) (McWilliams, 2016). Such structures have been found to drive vertical heat fluxes, statistically upward, thus acting to restratify the upper oceanic layers (Boccaletti et al., 2007; Fox-Kemper et al., 2008; Lapeyre et al., 2006; McWilliams et al., 2009; Tandon & Garrett, 1994, 1995). However, Su et al. (2018), using a global numerical model with a high spatial resolution, found that MLIs and submesoscale fronts in high energetic regions, such as the Gulf Stream, the Kuroshio Extension, and the Antarctic Circumpolar Current, produce upward vertical heat fluxes with a magnitude much larger than suggested by previous studies, thus further warming the ocean surface and cooling deeper layers over depths of 200 to 500 m. This magnitude reaches up to 200 W m^{-2} in wintertime at midlatitudes when averaged over 3 months. Such magnitudes have been later confirmed by some in situ experiments (Siegelman et al., 2020; Yu et al., 2019). These submesoscale vertical heat fluxes, when integrated over the whole ocean and yearly averaged, lead to a global vertical heat transport of ~3.5 PW, causing a sea surface warming of 0.3°C at midlatitudes and a resulting heat release from the ocean to the atmosphere of O(10) W m^{-2} (Su et al., 2018). Such submesoscale contribution to vertical heat transport, much larger than the 1-PW magnitude previously reported using parameterizations of submesoscale contribution (Griffies et al., 2015), competes with the major contributors of vertical heat transport (Griffies et al., 2015; Wolfe et al., 2008).

Su et al. (2018) have estimated submesoscale vertical heat fluxes using vertical velocity and temperature anomalies, each averaged over 1 day. These fluxes are hereafter referred to as low-frequency (LF) vertical heat fluxes. The choice of not explicitly estimating the impact of motions with frequencies higher than 1 day^{-1} (high frequency or HF) was based on the assumption that these HF motions principally concern internal gravity waves (IGWs) that experience a direct kinetic energy cascade (through nonlinear interactions) leading ultimately to turbulent mixing. Therefore, climate models that do not resolve these HF motions parameterize their impact on vertical heat fluxes as diffusive processes associated with the breaking of IGW (Griffies et al., 2015, Wolfe et al., 2008). This assumption may be questioned by recent findings (Siegelman, 2020; Thomas, 2017) that suggest HF motions may drive an upward heat transport. Such contribution to vertical heat fluxes is explained either by HF motions that are not waves but submesoscale balanced motions associated with Rossby number of order O(1) (i.e., frequencies larger than the Coriolis frequency, f) (McWilliams et al., 2009; Thomas et al., 2008) or/and by the interactions between IGWs and these HF balanced motions (Barkan et al., 2017; Rocha et al., 2018; Thomas, 2017). These findings prompted us to revisit our vertical heat transport study in the global ocean by quantifying the impact of motions with frequencies higher than 1 day^{-1}.

We use the same numerical model with a high spatial resolution (1/48°, 90 vertical levels) as in Su et al. (2018) to produce an assessment of the HF heat transport in the global ocean. The new result of the present study is to show that HF motions drive a significant upward heat transport in winter associated with submesoscale thermal fronts located around and in-between mesoscale eddies. The magnitude of this transport in the global ocean is equal to or larger than the one explained by LF submesoscale motions found in Su et al. (2018). The next section summarizes the main characteristics of the global ocean model used and the methodology employed to discriminate between LF and HF vertical heat fluxes. Results are detailed in section 3. A discussion of the possible physics explaining our results is offered in section 4. The last section summarizes our results.

2. Methods

To assess the impact of small-scale and high-frequency motions on vertical heat transport in the upper ocean over periods of O (months to years), we use a unique simulation, called LLC4320, with an unprecedented spatial resolution for a global model (1/48°, 90 vertical levels), detailed in supporting information Text S1 (Large et al., 1994, 1997; Large & Yeager, 2004; Menemenlis et al., 2008; Rocha et al., 2016). We present the resolved advective vertical heat fluxes at 0.1–0.5° scale range (degree in terms of longitude), using widely applied spatial and temporal filters (supporting information Text S2; Capet, Campos, & Paiva, 2008; Capet et al., 2008b; Su et al., 2018; Uchida et al., 2017). Here 0.1° is roughly the physically resolved length scale captured by the simulations, which is usually estimated at 5 times the numerical resolution (1/48° in this study). Here 0.5° (~ 50 km at mid-latitudes) is chosen as the upper bound of the length scale to quantify the heat

flux. This is because motions at scales smaller than 0.5° are typically not resolved by current climate models, and therefore, it is important to explicitly evaluate the associated flux at these scales. The diagnosed heat flux in this study only includes the advective flux resolved by this simulation (0.1–0.5° scale range) and does not include parameterized fluxes, for example due to convection.

We derive the HF contribution by obtaining the vertical heat fluxes from snapshots provided at every hour (including both HF and LF contributions) and then subtracting a LF contribution, which is calculated from the daily average of the hourly snapshots. We have found that the HF contribution of vertical heat fluxes is principally explained by submesoscales, as confirmed by the frequency-wavenumber vertical heat fluxes cospectra (Figure 6). Thus, when referring to HF in our study, we implicitly refer to spatial scales <0.5°, that is, submesoscales. These scales are resolved in only high-resolution numerical models and not in climate models. Such HF flux is found to be large in winter and weak in summer.

3. Results

3.1. Global Impact of HF Heat Fluxes

The global distribution and magnitude of HF and LF vertical heat fluxes explained by submesoscales, when averaged over 3 months during winter, are displayed in Figure 1 with the LF contribution (Figure 1a) identical to the one reported in Su et al. (2018). The HF contribution (Figure 1b), which represents the primary new result of this study, has a global distribution similar to the LF contribution (Figure 1a), that is, principally intensified in high-eddy kinetic energy (EKE) regions at midlatitudes, such as the Kuroshio Extension, Gulf Stream, and Antarctic Circumpolar Current, as well as in the Northeastern Atlantic. The similarity between HF and LF contributions is confirmed by a pointwise comparison that leads to a correlation of 0.81. The HF contribution makes the total vertical heat fluxes (LF + HF contributions) to reach magnitudes of up to 500 W m^{-2} at 40 m (when averaged over a 3-month period and a 300-km box size) in the Kuroshio Extension and the Antarctic Circumpolar Current (Figure 2a). When zonally averaged over the global ocean, total vertical heat fluxes are mostly trapped within the first 200 m at midlatitudes but can reach a depth of up to 1,000 m in the Northern Hemisphere (Figure 2c). HF contribution is systematically larger than the LF contribution in high-EKE regions, by a factor of almost 2, but smaller in subtropical gyres as emphasized by Figures 2b and 2d. This last result may be explained by our methodology that may not appropriately discriminate HF motions from LF motions in low latitudes. However, since the total vertical heat fluxes at submesoscale are quite weak in these low latitudes, this does not change our conclusions for the global ocean. The HF contribution to vertical heat fluxes in summer (not shown) is negligible as is the LF submesoscale contribution (Su et al., 2018). As a general pattern, the ratio of HF vertical heat fluxes to the LF vertical heat fluxes increases with latitude (Figure 2b); this is partly due to the fact that the dynamic frequency of eddy motions typically increases with latitude.

Integration of the total (LF + HF) vertical heat fluxes explained by submesoscales over the global ocean leads to an upward vertical heat transport, during winter, with a magnitude of 13.7 PW at 40-m depth, equivalent to a global average flux of 37.8 W m^{-2}. The corresponding annual mean vertical heat transport is roughly half of wintertime values, which corresponds to almost 7 PW at 40 m. Such submesoscale contribution is large enough to be an important component in modulating the ocean's net heat uptake. Indeed, it is almost 5 times larger than the upward mesoscale eddy contribution (see Su et al., 2018) in the top 400 m. The submesoscale flux that is directly resolved by this simulation is more than 7 times larger than that estimated using parameterizations that only take into account MLIs (Fox-Kemper et al., 2011; Griffies et al., 2015). This difference suggests a need to consider other processes or revisit these parameterizations. In addition, the annual mean submesoscale heat flux near the surface (~20 W m^{-2}) is comparable to the global ocean latent and sensible heat fluxes (90 and 10 W m^{-2} respectively). This further emphasizes that the vertical transport explained by submesoscales, and in particular the HF contribution, that represents a little more than 50% of this transport, is a significant component of the global ocean heat budget.

The submesoscale contribution to the upward vertical heat transport will be balanced or competed by other contributions, such as the downward heat flux due to the large-scale wind-driven vertical circulation and small-scale diffusive processes as well as the upward contributions of mesoscale eddies and convective adjustment (Griffies et al., 2015; Wolfe et al., 2008). Although the order of magnitude of the submesoscale contribution found here is similar to other contributions (see Figure 12 in Griffies et al., 2015), it is

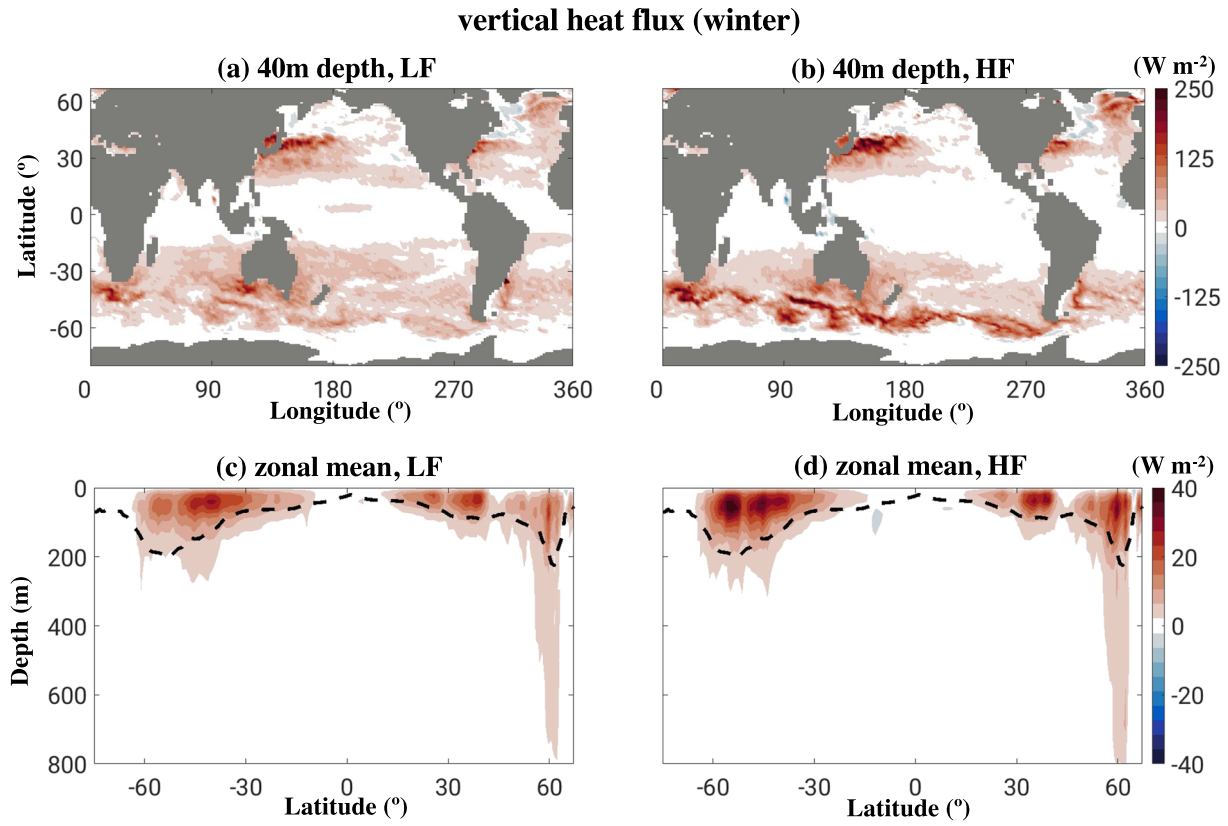

Figure 1. Global patterns of the wintertime vertical heat flux associated with scales <0.5° (~50 km in midlatitudes, submesoscales). Wintertime refers to January–March in the Northern Hemisphere and July–September in the Southern Hemisphere. Values are spatially smoothed over 3° × 3° square boxes; positive values indicate upward. (a) Wintertime vertical heat flux at 40-m depth, calculated from daily mean model output (low-frequency, LF component). (b) As in panel (a) but for the difference between heat fluxes calculated from hourly output and from daily mean output (high-frequency, HF component). (c) Zonal mean wintertime vertical heat flux, calculated from daily mean model output (LF component). Dashed curves denote the wintertime zonally averaged mixed-layer depth (MLD) (black), using a potential density difference criteria of 0.03 kg m^{-3}. (d) As in panel (c) but for the difference between the vertical heat fluxes calculated from hourly output and from daily mean output (HF component).

beyond the scope of this study to diagnose all of these components (as done in Griffies et al., 2015; Wolfe et al., 2008, and later studies). Indeed, the present numerical simulation has been integrated at high resolution just for 14 months, and therefore, the large-scale circulation is not yet equilibrated (although the simulation's mesoscale EKE compares well with observations, as reported in Torres et al., 2018). Such equilibrium, as emphasized in Griffies et al. (2015) and in particular in the double-gyre study of Lévy et al. (2010) that explicitly takes into account submesoscales (see their Figure 2), requires an integration over at least a decadal time scale to account for the impact of submesoscale structures on the large-scale circulation via energy transfer through mesoscale eddies (Dong et al., 2020; Qiu et al., 2014; Sasaki et al., 2014).

Nevertheless, the present results highlight the fundamental role of submesoscales, and in particular their HF component, on the upward vertical heat transport in winter, and therefore on the transient (seasonal) ocean heat uptake in the top 400 m. The mechanisms that support a HF heat flux of this magnitude remain an open question. To better understand these mechanisms, the next subsections describe the vertical heat fluxes characteristics in physical and spectral spaces.

3.2. Localization of HF Heat Fluxes in Physical Space

As illustrated in the Kuroshio Extension region (Figure 3a), high-EKE regions are characterized by the presence of energetic submesoscale filaments of relative vorticity, many of them located at the periphery of and in-between mesoscale eddies (see the black box in Figure 3a). These filaments are stretched by the eddy strain field and are usually associated with strong density gradients that, throughout most of the ocean,

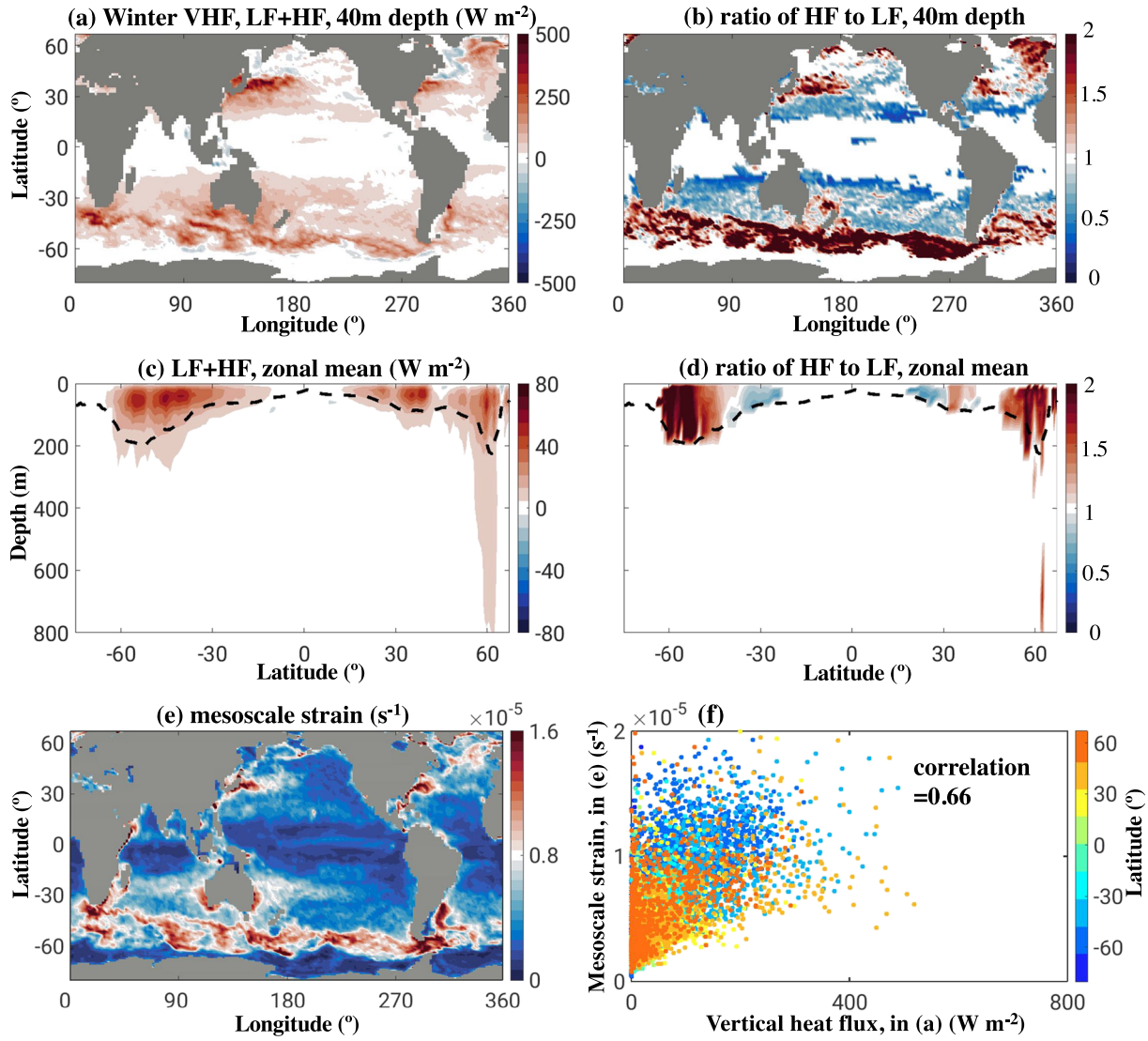

Figure 2. (a and c) Same as Figures 1a and 1c but for the total vertical heat flux (VHF) including both low frequencies and high frequencies (LF + HF), at 40-m depth and of the zonal averaging, respectively. (b and d) The ratio of HF vertical heat fluxes to the LF vertical heat fluxes at 40-m depth and of the zonal average, respectively. (e) Surface mesoscale strain rate in winter. Areas with large mesoscale strain generally correspond to a high flux (panel e vs. panel a) and a high ratio of HF to LF (panel e vs. panel b). (f) Scatter plot between mesoscale strain shown in panel e and vertical heat fluxes shown in panel (a), with a correlation coefficient $r = 0.66$.

correspond to thermal fronts (Su et al., 2018). As further displayed in Figures 3b, 3c and 4, these submesoscale fronts are the structures where both LF and HF vertical heat fluxes, averaged over 1 week, have the largest magnitude. These fronts and their associated vertical heat fluxes can reach depths down to 400 m (Figures 3d and 3e). Both LF and HF weekly averaged contributions to vertical heat fluxes are positive (upward), with a local magnitude reaching ~1,000 W m^{-2} (Figures 3b–3e and 4), with the HF magnitudes being even larger (Figures 3b, 3c, and 4). These characteristics suggest that HF vertical heat fluxes may be driven by the same dynamics as the LF fluxes, that is, associated with strong thermal fronts and strong relative vorticity within strain dominated areas. Such frontal dynamics around and in-between eddies and its impact on the vertical heat fluxes involving HF is revisited and discussed in Siegelman et al. (2020) (see their Figure 12) but also has been revealed in some recent in situ experiments (Siegelman et al., 2020; Yu et al., 2019).

The localization of vertical heat fluxes in strain dominated regions in winter is confirmed by the scatterplot between these fluxes and the strain rate in the global ocean (Figure 2f). The correlation between the two

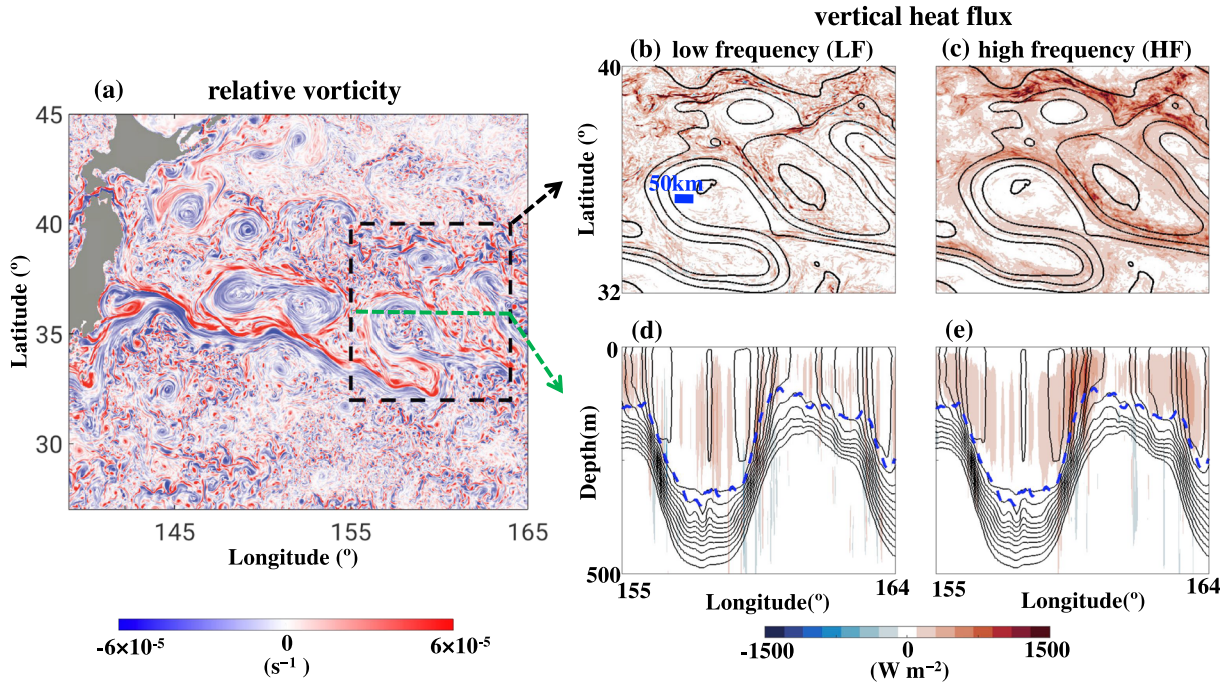

Figure 3. (a) Surface relative vorticity in the Kuroshio Extension on 4 February 2012. (b) Low-frequency (LF) vertical heat flux associated with scales <0.5° at 40-m depth, corresponding to the black dashed box in panel (a). Values are averaged over the period 1–7 February and are calculated using daily mean model output: the LF component. Positive values represent upward fluxes; contours show isolines of sea surface height (SSH) with a 0.2-m contour spacing, indicating mesoscale eddies. (c) As in panel (b) but for the difference in vertical heat flux between those calculated from hourly snapshots and from daily mean output: the high-frequency (HF) component. The sum of panels (b) and (c) is the heat flux calculated from hourly snapshots. (d and e) As in panels (b) and (c) but for vertical sections along ~36°N as shown by the green dashed line in panel (a). The contours indicate isopycnals, indicating the heat fluxes are focused in regions with large lateral density gradients. The mixed-layer depth, defined based on a potential density difference criteria of 0.03 kg m^{-3} (de Boyer Montégut et al., 2004), is shown by the dashed blue curve.

fields is 0.66. One interesting result, emphasized by the comparison of Figures 2a, 2b, and 2e, is that HF vertical fluxes are usually larger than LF ones in regions where the strain rate is larger than ~1 day^{-1}. This further emphasizes the impact of the strain field on the emergence of HF vertical heat fluxes.

3.3. Temporal Variations of HF Heat Fluxes

Time series of LF vertical heat fluxes (averaged over 100-km × 100-km boxes) in high-EKE regions exhibit intermittency at daily to weekly time scales as well as a strong seasonality (red curves in Figures 5a–5e), consistent with Su et al. (2018). Time series of daily averaged HF vertical heat fluxes (blue curves in Figures 5a–5e) strongly covary with anomalies of LF fluxes in all regions (HF vs. LF; Figures 5a–5e), especially during winter. In all regions, the correlations between the two time series is larger than 0.7. This similar variability confirms the close connection between the processes producing HF and LF fluxes. Amplitudes of HF fluxes are typically larger than LF fluxes (up to 500–1,000 W m^{-2}) in the Kuroshio Extension and the Southern Ocean (Figures 5a and 5e), but both components are almost similar in the North Atlantic and the Agulhas Current (Figures 5b and 5d). The HF amplification of vertical heat fluxes is associated with an increase in the temporal correlation between vertical velocity and temperature: from 0.24 to 0.42 when using the hourly model output (LF + HF), as compared to the LF output. Thus, HF and LF vertical heat fluxes are highly correlated both in space and time, suggesting the mechanisms that drive them are similar.

3.4. Heat Flux Characteristics in Spectral Space

Model outputs allow for the exploration of the variance partition of any quantity in terms of frequencies (ω) and wavenumbers (k), with k the modulus of the horizontal wavenumber. We take advantage of these outputs to infer the location of vertical heat fluxes in spectral space. To do so, we have estimated the vertical heat fluxes cospectrum as detailed in Appendix A (Torres et al., 2018). As already noted in Torres et al. (2018), the ω-k space includes two regions separated by the dispersion relation curve associated with the highest

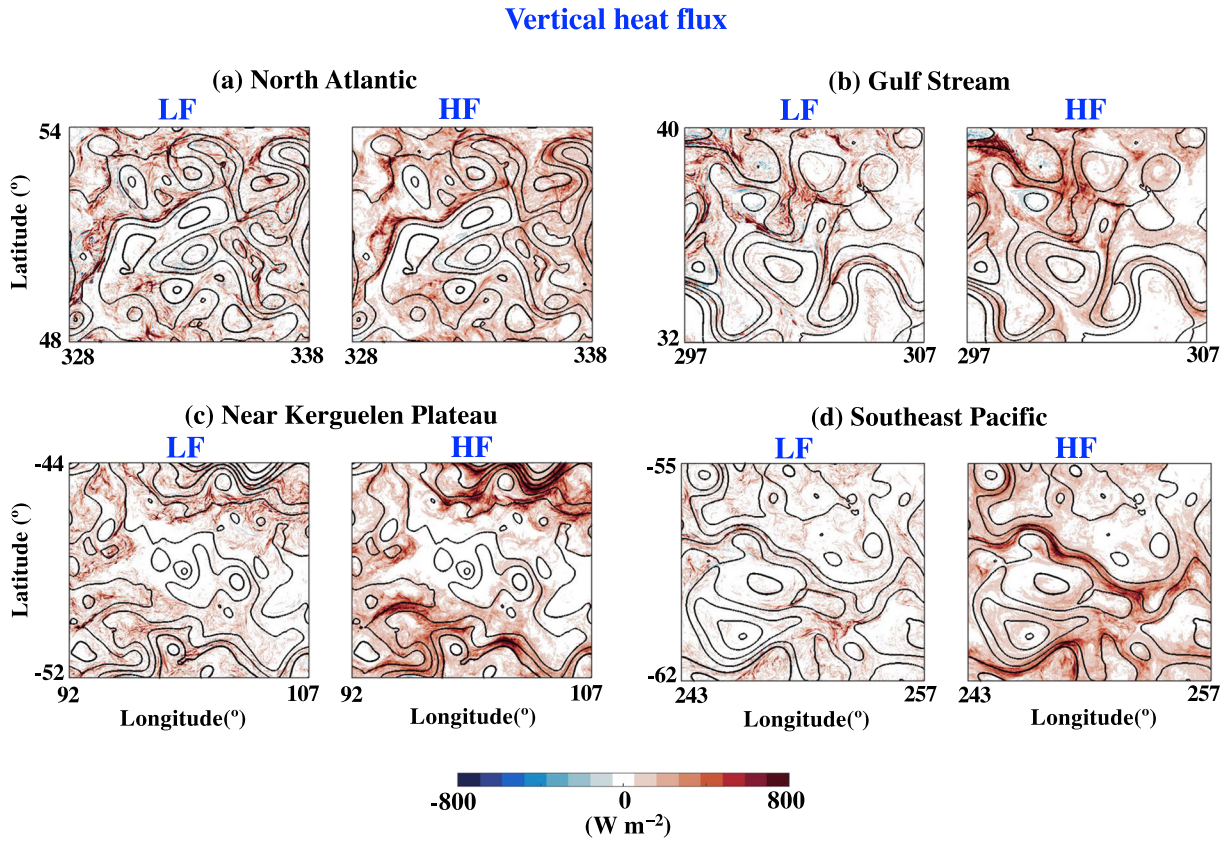

Figure 4. Same as Figures 3b and 3c but for other regions in the world ocean: (a) North Atlantic, (b) Gulf Stream, (c) Near Kerguelen Plateau, and (d) Southeast Pacific, at 40-m depth. (a) and (b) are averaged over 1–7 February, and (c) and (d) are averaged over 1–7 August, corresponding to wintertime. These panels confirm the colocation of HF with LF flux around the edge of mesoscale eddies (contours) and the fact that the HF nearly doubles the magnitude of vertical heat fluxes.

baroclinic mode taken into account in the model (dashed curve in Figure 6a). The spectral fluxes above and on the left of this curve are explained by the contribution of linear IGWs. The spectral fluxes below and on the right of the dashed curve are explained by contribution of the balanced motions (i.e., motions in geostrophic or gradient-wind balance) and contribution of unbalanced motions including nonlinear IGWs. The ω-k vertical heat fluxes cospectra for the Kuroshio Extension (Figures 6b and 6c) are representative of most of the global ocean (see Figure 7, for other regions). We have checked in all regions that the Parseval relation is verified; that is, integration of the cospectrum over all frequencies and wavenumbers leads to the same number as vertical heat fluxes integrated over the physical domain for three months. This relation has also been checked for HF ($\omega > 1$ day^{-1}) and LF ($\omega < 1$ day^{-1}) vertical heat fluxes. Vertical heat fluxes cospectra are shown in a variance preserving form.

As a preliminary, it is useful to mention recent results related to HF motions in the spectral space using numerical outputs. Rocha et al. (2016) and Torres et al. (2018) found that, in summer, the variance of HF motions is principally distributed along the dispersion relation curves associated with IGWs. Moreover, as reported and explained by Rocha et al. (2016) and Lahaye et al. (2018), IGWs in summer are more energetic within the mixed layer than in winter in most of the regions of the world ocean. On the other hand, in winter, a large part of the variance of HF motions is found in the region to the right of the dispersion relation curve associated with the highest baroclinic mode. Thus, in summer, HF motions seem to be principally explained by the contribution of IGW. In winter, HF motions involve energetic motions at smaller spatial scales that may result from nonlinear mechanisms as discussed in the next section.

During winter, the contribution to vertical heat fluxes from IGW is very weak (Figure 6b). vertical heat fluxes at 40 m are principally explained by motions (below and at the right of the dashed curve) with spatial scales

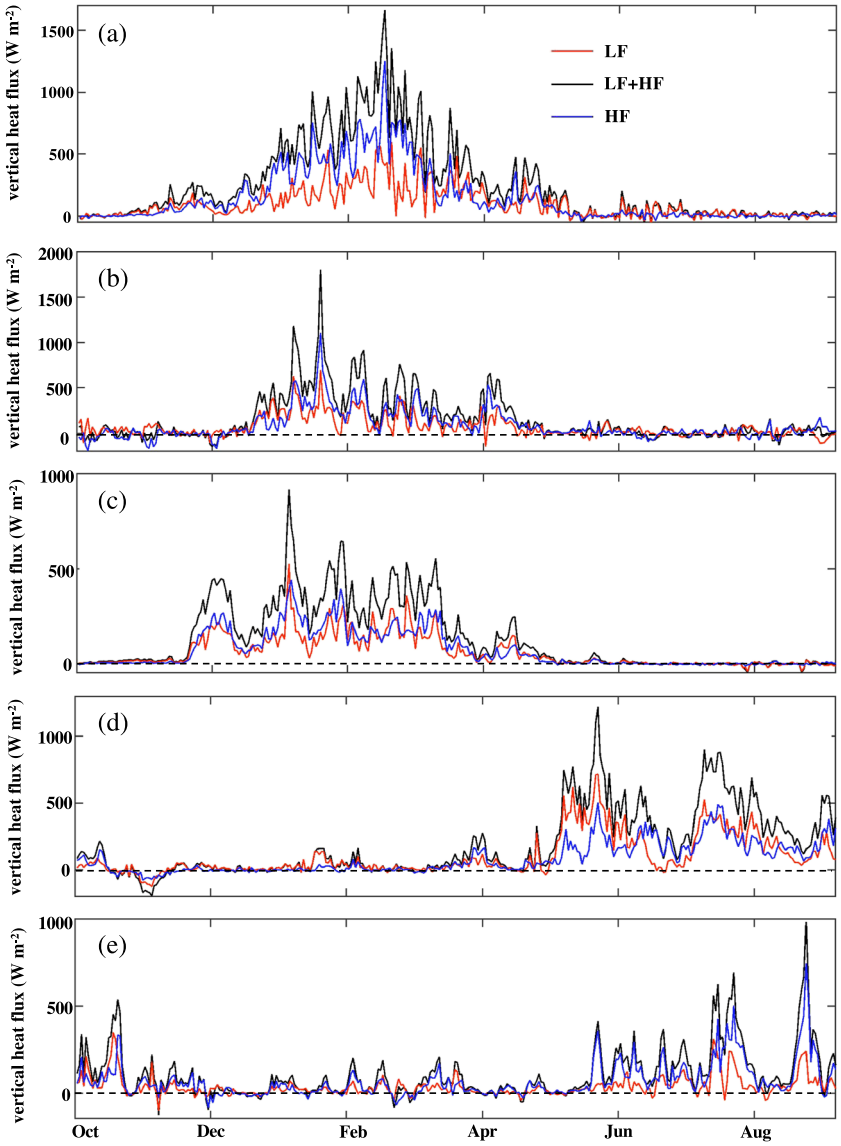

Figure 5. Time series of vertical heat flux associated with scales <0.5° at 40-m depth. Curves indicate heat fluxes calculated from daily mean model output (red, low-frequency or LF), hourly snapshots (black, low-frequency + high-frequency, or LF + HF), and the difference between the two (blue, high-frequency or HF). The LF + HF time series have been daily averaged for easier comparison. Heat flux calculations are from a 1° × 1° box centered at a given location in each region. Panels (a) to (e), respectively, refer to the Kuroshio Extension (box centered at 39°N, 158°E), the Gulf Stream (box centered at 39°N, 66°W), (b) Northernmost Atlantic (box centered at 58°N, 24°W), (c) Agulhas Current (box centered at 43°S, 14°E), and (d) the Southern Ocean (box centered at 50°S, 87°E).

mostly smaller than 0.5° (~50 km in midlatitudes), which corroborates the 0.5° filter used in previous sections. Vertical heat fluxes in this spectral region is principally positive and distributed broadly and continuously across both HF ($\omega > 1$ day^{-1}) and LF ($\omega < 1$ day^{-1}). The variance associated with the HF contribution is larger than the LF contribution, as found in physical space, and involves smaller scales (<0.5°). At 200 m depth (Figure 7), the relative contribution of mesoscale eddies (spatial scales >0.5°) can be larger than submesoscales, as expected. Both at 40 and 200 m depths, there is a continuity between HF and LF contributions that closely follows a nondispersive line: $\omega - ck = 0$, with $c \approx 10$ cm s^{-1}. Thus, HF and LF vertical heat fluxes in winter occupy different regions of the spectral space, with HF vertical heat fluxes being associated not only with shorter time scales (by definition) but also with smaller spatial scales than LF vertical heat fluxes.

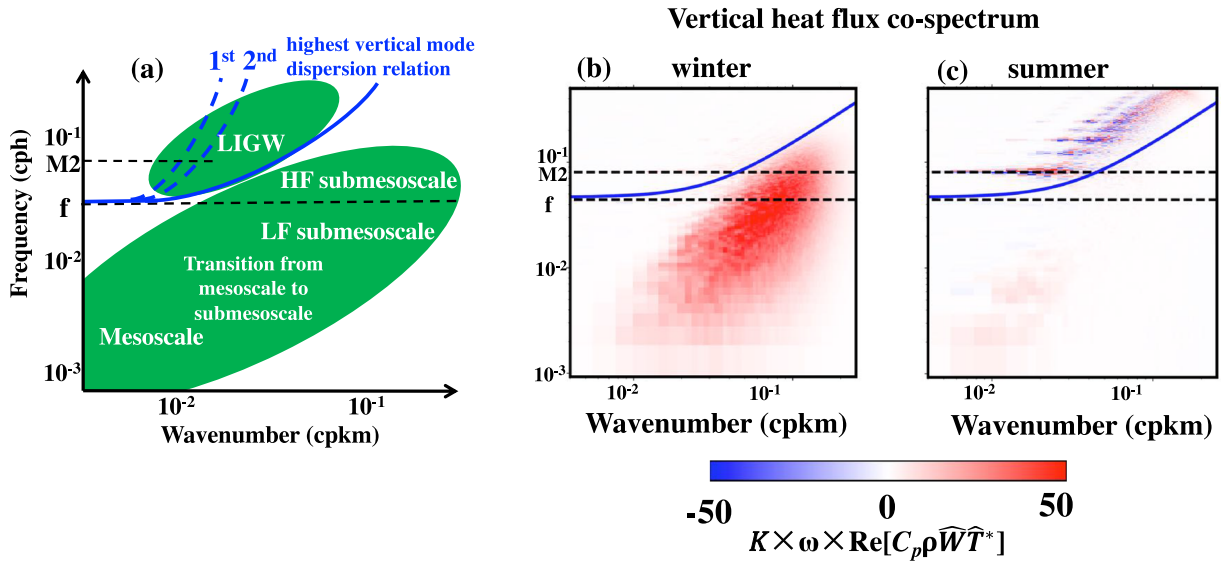

Figure 6. (a) Schematic representation of oceanic motions in frequency-wavenumber space (given as cycles per hour, cph, and cycles per km, cpkm). LIGW denotes linear internal gravity waves; M2 denotes the M2 tidal frequency; f is the Coriolis frequency. The IGW dispersion relations are indicated by blue curves; the first, second, and highest vertical modes are plotted. (b) Frequency-wavenumber cospectrum of the vertical heat flux at 40-m depth during winter (January–March) and (c) summer (July–September), within the Kuroshio Extension region (black dashed box in Figure 3a). The cospectra density ($Re[C_p \rho \hat{W} \hat{T}^*]$, unit: W m^{-2} cph^{-1} $cpkm^{-1}$) are shown in a variance preserving form; that is, they are multiplied by the wavenumber and frequency to compensate for logarithmic shrinking on both axes. The blue curves show the IGW dispersion curve for the tenth baroclinic mode—the highest resolved by the simulation (Torres et al., 2018).

The vertical heat fluxes cospectrum strongly differs in summer (Figure 7). Vertical heat fluxes become non-negligible in the IGW region where these fluxes are mostly distributed along the dispersion relation curves associated with the different baroclinic modes with both positive and negative values. Vertical heat fluxes averaged over the IGW region are negligible. Small positive vertical heat fluxes values are found in the balanced motion region, but they mostly are associated with mesoscales and frequencies lower than f.

4. Discussion

It remains difficult to infer the mechanisms responsible for the emergence of HF winter vertical heat fluxes in the range of spatial scales <0.5° (~50 km), using spectral characteristics alone. One explanation for the variance at high frequencies would be to invoke the Doppler shift mechanism, since the HF contribution is aligned with the LF one following a nondispersive line, as mentioned above (see also Balwada et al., 2018). We do not reject this idea (Doppler shift mechanism), but we have not yet found a robust argument to explain why this effect would give rise to an enhanced HF vertical heat fluxes in the winter, but not in the summer. Alternatively, combining the vertical heat fluxes characteristics in physical space with those in spectral space suggests that either the ageostrophic character of submesoscale fronts, reported in recent studies (Siegelman, 2020), or the nonlinear interactions between IGWs and balanced motions within such ageostrophic submesoscale fronts (see Thomas, 2017, for a review) could give rise these large HF values.

Since Hoskins and Bretherton (1972), it is known that thermal fronts are associated with large Rossby number and small Richardson number (see Molemaker et al., 2005, 2010; Thomas et al., 2008, for the ocean). In situ experiments of the past 10 years in different parts of the world ocean (Shcherbina et al., 2013; Siegelman et al., 2020; Thompson et al., 2016; Viglione et al., 2018; Yu et al., 2019) have confirmed that submesoscale thermal fronts, embedded in a strain field, exhibit scales much smaller than 50 km (i.e., ~5–10 km) and are characterized by large Rossby numbers (and therefore frequencies larger than f) and small Richardson numbers. The existence of such strongly ageostrophic fronts is consistent with the large variance found in the ω-k spectrum of relative vorticity and vertical velocity in the region to the right of the dashed curve for $\omega > f$ and for spatial scales smaller than 50 km as reported by Torres et al. (2018) and Siegelman et al. (2020). Then, it is

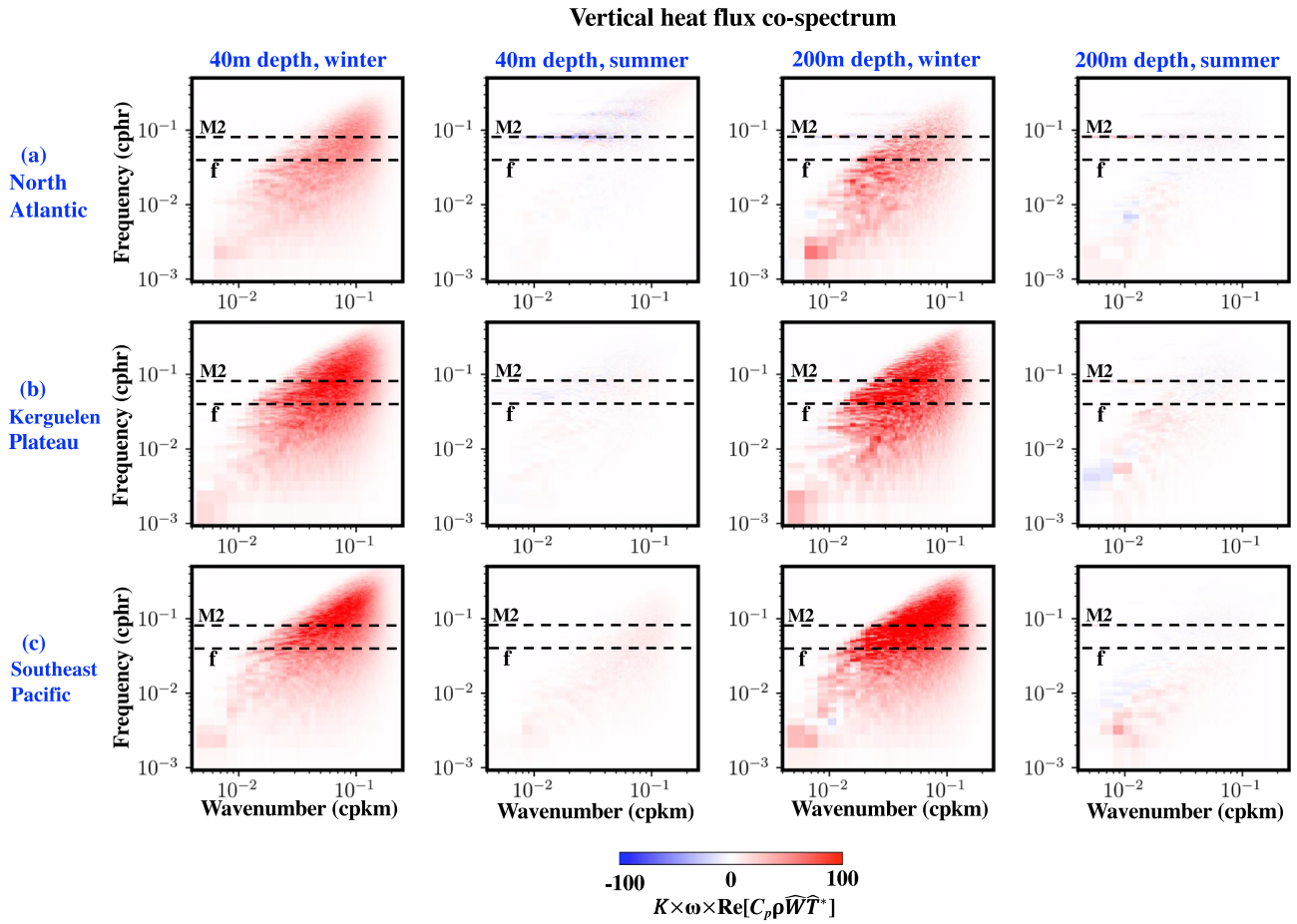

Figure 7. Same as Figures 6b and 6c but for more examples in other ocean regions: (a) North East Atlantic (48–54°N, 328–338° longitudes), (b) Kerguelen (44–52°S, 92–107° longitudes), and (c) South East Pacific (55–62°S, 243–257° longitudes), in winter and summer, at 40- and 200-m depths. Wintertime is represented by January–March and July–September in the Northern Hemisphere and Southern Hemisphere, respectively, while summertime is represented by July–September and January–March in the Northern Hemisphere and Southern Hemisphere, respectively. The cospectra density ($Re[C_p\rho\widehat{W}\widehat{T}^*]$, unit: W m^{-2} cph^{-1} $cpkm^{-1}$) are multiplied by the wavenumber (K, unit: cpkm) and frequency (ω, unit: cph) to compensate for logarithmic shrinking on both axes.

plausible that large vertical heat fluxes are found in this spectral region with large frequencies and large wavenumbers.

The continuity of the heat flux across HF and LF parts of frequency-wavenumber space (Figures 6 and 7), as well as their collocation in submesoscale fronts (Figures 3 and 4) and their highly coherent temporal variability (Figure 5), may suggest the possibility that submesoscale motions of both the LF and HF components simply comprise a single class of dynamics, with varying degrees of "balance" as the space and time scales vary.

In addition, recent theoretical findings (Barkan et al., 2017; Rocha et al., 2018; Taylor & Straub, 2016; Thomas, 2017; Xie & Vanneste, 2015) suggest that these large upward vertical heat fluxes may be further stimulated at HF in the presence of IGW. Indeed, large Rossby numbers and low Richardson numbers are known to impact the IGW dispersion relations (Kunze, 1985) and therefore the IGW propagation and polarization within fronts. A consequence is that IGWs may be trapped in density fronts and become polarized in the cross-front direction with their horizontal wavenumbers increasing. In this process, as detailed in Thomas (2017) and confirmed by Barkan et al. (2017) and Rocha et al. (2018), there is an energy transfer, driven by the strain field, from balanced motions to IGWs and ultimately from IGWs to the ageostrophic motions associated with thermal fronts, leading to an enhanced vertical velocity at HF and very small spatial scales. This may also contribute to an enhanced HF vertical heat fluxes found in this study.

5. Conclusion

The present results extend those of Su et al. (2018) by including the impact of HF motions on the vertical heat transport in the global ocean. They indicate that motions with small spatial and temporal scales (respectively, <0.5° and <1 day) have a significant impact on the vertical heat transport and therefore on the ocean's net heat uptake. This HF submesoscale component reaches a large magnitude of about 7 PW over the global ocean during winter at 40-m depth and also large locally even down to 800-m depth (Figure 1d); thus, it competes with the other major components, namely, the large-scale wind-driven vertical circulation, mesoscale eddies, and small-scale diffusive processes. Not surprisingly, the HF submesoscale component, similar to the LF one, is located in submesoscale fronts (< 0.5°, ~50 km at midlatitudes).

The dynamics giving rise to the submesoscale component is consistent with the frontogenesis of submesoscale thermal fronts, as already discussed in Su et al. (2018) and recently confirmed by in situ experiments (Siegelman et al., 2020, Yu et al., 2019). The mechanisms involved in the HF contribution still need to be deciphered. It is possible that the HF flux and LF flux are generated by the same class of mechanisms, as suggested by their similarity of spatial and temporal characteristics (Figures 1, 3, 4, 5). Invoking the strong ageostrophic character of submesoscale fronts as discussed in Thomas et al. (2008) and their interactions with IGWs (see Thomas, 2017) seems to be another pertinent avenue to consider. Exploration of this avenue should be the purpose of future work.

Our ocean global model at very high resolution has been integrated for only 14 months. Such global integration is at the limit of the current existing computer capacity. Longer time integration will be needed in the future, when we have access to exascale computers, to assess more accurately the submesoscale component of the vertical heat transport and its impacts. However, the present results stress that this component, and in particular its HF part, should not be ignored in future climate models. If not explicitly resolved, this component may need to be parameterized using a dynamical approach that takes into account more dynamics of submesoscale fronts. At last, in situ observations at high spatial and temporal resolutions are highly useful to better understand the mechanisms involved.

One question to investigate is the impact of these vertical heat fluxes driven by submesoscale thermal fronts on the air-sea interactions and the coupled ocean-atmosphere system. Indeed, submesoscale (and mesoscale) sea surface temperature (SST) fronts are known to trigger significant wind divergence that stimulates locally the turbulent latent and sensible heat fluxes in the atmosphere (Foussard et al., 2019a, 2019b; Small et al., 2019; Yang et al., 2019). High-resolution coupled models may be needed to address this question.

Appendix A: Vertical Heat Flux in the Spectral Space

The frequency (ω)-wavenumber (k) cospectra of vertical heat fluxes are calculated as

$$VHF = Re\left[C_p\rho\widehat{W}\widehat{T}^*(k,\omega)\right],$$

where $\hat{W}$ is the Fourier transform of the vertical velocity, $\hat{T}^*$ is the conjugate of the Fourier transform of the potential temperature, C_p is the heat capacity of the sea water, and ρ is the potential density. Before computing the ω-k cospectrum, the mean and linear trend in space and time of W and T were removed. Subsequently, both detrended variables were multiplied by a 3-D (x, y, t) Hanning window (see the supporting information for a detailed description of the cospectrum). The cospectrum was calculated in 6° latitude × 6° longitude boxes and 3-month hourly output. This permit to resolve wavelengths from ~4 to ~300 km and periods from 2 hr to 45 days. The spectrum was azimuthally integrated in wavenumber space in order to express the cospectrum in terms of the modulus of the horizontal wavenumber k.

We calculate vertical heat fluxes in four regions with distinct ocean dynamics but showing seasonality (Su et al., 2018; Torres et al., 2018): Kuroshio Extension, North Atlantic, Kerguelen Plateau, and Southeast Pacific. The cospectra density ($Re[C_p\rho\widehat{W}\widehat{T}^*]$, unit: W m^{-2} cph^{-1} cpkm^{-1}) are shown in a variance preserving form; that is, they are multiplied by the wavenumber and frequency to compensate for logarithmic shrinking on both axes (Torres et al., 2018).

Data Availability Statement

The model and data used in this study can be obtained/reproduced from the MITgcm website (http://wwwcvs.mitgcm.org/viewvc/MITgcm/MITgcm_contrib/llc_hires/llc_4320/).

Acknowledgments
We gratefully thank the MITgcm developers and NAS scientists who made it possible to run our global numerical simulation at high resolution, as well as Christopher Henze at NASA Ames Hyperwall for providing insightful and unique visualization capabilities. We thank Hong Zhang for the excellent technical support on conducting the numerical simulation. Z. S. was supported by NSF Award OAC-1835618 (Collaborative Research: Framework: Data: Toward Exascale Community Ocean Circulation Modeling) and NASA Grant NNX15AG42G. P. K. is supported by the NASA-CNES SWOT mission and a NASA Senior Fellowship. A. F. T. is supported by NASA Grants NNX15AG42G and 8ONSSCI9KIOO4. J. W. was supported by the SWOT mission and JPL President/Director Research and Development Fund. C.H. was supported by NSF Award OAC-1835618. H.T., L.S., J.W. and D.M. carried research at the Jet Propulsion Laboratory, California Institute of Technology, under contract with NASA, with support from the Physical Oceanography (PO) and Modeling, Analysis, and Prediction (MAP) Programs. Computations were carried out at the NASA Advanced Supercomputing (NAS) facilities.

References

Balwada, D., Smith, K. S., & Abernathey, R. (2018). Submesoscale vertical velocities enhance tracer subduction in an idealized Antarctic circumpolar current. *Geophysical Research Letters*, *45*, 9790–9802. https://doi.org/10.1029/2018GL079244

Barkan, R., Winters, K. B., & McWilliams, J. C. (2017). Stimulated imbalance and the enhancement of eddy kinetic energy dissipation by internal waves. *Journal of Physical Oceanography*, *47*(1), 181–198.

Boccaletti, G., Ferrari, R., & Fox-Kemper, B. (2007). Mixed layer instabilities and restratification. *Journal of Physical Oceanography*, *37*(9), 2228–2250.

de Boyer Montégut, C., Madec, G., Fischer, A. S., Lazar, A., & Iudicone, D. (2004). Mixed layer depth over the global ocean: An examination of profile data and a profile-based climatology. *Journal of Geophysical Research: Oceans*, *109*, C12003. https://doi.org/10.1029/2004JC002378

Callies, J., Flierl, G., Ferrari, R., & Fox-Kemper, B. (2016). The role of mixed-layer instabilities in submesoscale turbulence. *Journal of Fluid Mechanics*, *788*, 5–41.

Capet, X., Campos, E., & Paiva, A. (2008). Submesoscale activity over the Argentinian shelf. *Geophysical Research Letters*, *35*, L15605. https://doi.org/10.1029/2008GL034736

Capet, X., McWilliams, J. C., Molemaker, M. J., & Shchepetkin, A. (2008a). Mesoscale to submesoscale transition in the California current system. Part I: Flow structure, eddy flux, and observational tests. *Journal of Physical Oceanography*, *38*(1), 29–43.

Capet, X., McWilliams, J. C., Molemaker, M. J., & Shchepetkin, A. F. (2008b). Mesoscale to submesoscale transition in the California Current System. Part II: Frontal processes. *Journal of Physical Oceanography*, *38*(1), 44–64. https://doi.org/10.1175/2007JPO3672.1

Dong, J., Fox-Kemper, B., Zhang, H., & Dong, C. (2020). The seasonality of submesoscale energy production, content, and cascade. *Geophysical Research Letters*, *47*, e2020GL087388. https://doi.org/10.1029/2020GL087388

Ferrari, R. (2011). A frontal challenge for climate models. *Science*, *332*(6027), 316–317.

Ferrari, R., & Wunsch, C. (2009). Ocean circulation kinetic energy: Reservoirs, sources, and sinks. *Annual Review of Fluid Mechanics*, *41*(1), 253.

Foussard, A., Lapeyre, G., & Plougonven, R. (2019a). Response of surface wind divergence to mesoscale SST anomalies under different wind conditions. *Journal of the Atmospheric Sciences*, *76*(7), 2065–2082.

Foussard, A., Lapeyre, G., & Plougonven, R. (2019b). Storm tracks response to oceanic eddies in idealized atmospheric simulations. *Journal of Climate*, *32*, 445–463.

Fox-Kemper, B., Danabasoglu, G., Ferrari, R., Griffies, S., Hallberg, R., Holland, M., et al. (2011). Parameterization of mixed layer eddies. III: Implementation and impact in global ocean climate simulations. *Ocean Modelling*, *39*(1-2), 61–78. https://doi.org/10.1016/j.ocemod.2010.09.002

Fox-Kemper, B., Ferrari, R., & Hallberg, R. (2008). Parameterization of mixed layer eddies. Part I: Theory and diagnosis. *Journal of Physical Oceanography*, *38*(6), 1145–1165.

Griffies, S. M., Winton, M., Anderson, W. G., Benson, R., Delworth, T. L., Dufour, C. O., et al. (2015). Impacts on ocean heat from transient mesoscale eddies in a hierarchy of climate models. *Journal of Climate*, *28*(3), 952–977. https://doi.org/10.1175/JCLI-D-14-00353.1

Hoskins, B. J., & Bretherton, F. P. (1972). Atmospheric frontogenesis models: Mathematical formulation and solution. *Journal of the Atmospheric Sciences*, *29*, 11–37.

Klein, P., & Lapeyre, G. (2009). The oceanic vertical pump induced by mesoscale and submesoscale turbulence. *Annual Review of Marine Science*, *1*, 351–375.

Kunze, E. (1985). Near-inertial wave propagation in geostrophic shear. *Journal of Physical Oceanography*, *15*(5), 544–565.

Lahaye, N., Gula, J., & Roullet, G. (2018). Sea surface signature of internal tides. *Geophysical Research Letters*, *46*, 3880–3890. https://doi.org/10.1029/2018GL081848

Lapeyre, G., Klein, P., & Hua, B.-L. (2006). Oceanic restratification forced by surface frontogenesis. *Journal of Physical Oceanography*, *36*(2), 1577–1590.

Large, W. G., Danabasoglu, G., Doney, S. C., & McWilliams, J. C. (1997). Sensitivity to surface forcing and boundary layer mixing in a global ocean model: Annual-mean climatology. *Journal of Physical Oceanography*, *27*(11), 2418–2447.

Large, W. G., McWilliams, J. C., & Doney, S. C. (1994). Oceanic vertical mixing: A review and a model with a nonlocal boundary layer parameterization. *Reviews of Geophysics*, *32*(4), 363–403.

Large, W. G., Yeager, S. G. (2004). Diurnal to decadal global forcing for ocean and sea-ice models: The data sets and flux climatologies.

Lévy, M., Klein, P., Tréguier, A. M., Iovino, D., Madec, G., Masson, S., & Takahashi, K. (2010). Modifications of gyre circulation by sub-mesoscale physics. *Ocean Modelling*, *34*(1–2), 1–15. https://doi.org/10.1016/j.ocemod.2010.04.001

McWilliams, J. C. (2016). Submesoscale currents in the ocean. *Proceedings of the Royal Society A*, *472*(2189).

McWilliams, J. C., Colas, F., & Molemaker, M. J. (2009). Cold filamentary intensification and oceanic surface convergence lines. *Geophysical Research Letters*, *36*, L18602. https://doi.org/10.1029/2009GL039402

Menemenlis, D., Campin, J., Heimbach, P., Hill, C. N., Lee, T., Nguyen, A., et al. (2008). ECCO2: High resolution global ocean and sea ice data synthesis. *Mercator Ocean Quarterly Newsletter*, *31*, 13–21.

Molemaker, M. J., McWilliams, J. C., & Capet, X. (2010). Balanced and unbalanced routes to dissipation in an equilibrated easy flow. *Journal of Fluid Mechanics*, *654*, 35–63. https://doi.org/10.1017/S0022112009993272

Molemaker, M. J., McWilliams, J. C., & Yavneh, I. (2005). Baroclinic instability and loss of balance. *Journal of Physical Oceanography*, *35*, 1505–1517.

Qiu, B., Chen, S., Klein, P., Sasaki, H., & Sasai, Y. (2014). Seasonal mesoscale and submesoscale eddy variability along the North Pacific Subtropical Countercurrent. *Journal of Physical Oceanography*, *44*(12), 3079–3098. https://doi.org/10.1175/JPO-D-14-0071.1

Rocha, C. B., Chereskin, T. K., Gille, S. T., & Menemenlis, D. (2016). Mesoscale to submesoscale wavenumber spectra in drake passage. *Journal of Physical Oceanography*, *46*(2), 601–620. https://doi.org/10.1175/JPO-D-15-0087.1

Rocha, C. B., Wagner, G. L., & Young, W. R. (2018). Stimulated generation: Extraction of energy from balanced flow by near-inertial waves. *Journal of Fluid Mechanics*, *847*, 417–451.

Sasaki, H., Klein, P., Qiu, B., & Sasai, Y. (2014). Impact of oceanic-scale interactions on the seasonal modulation of ocean dynamics by the atmosphere. *Nature Communications*, *5*(1), 5636. https://doi.org/10.1038/ncomms6636

Shcherbina, A. Y., D'Asaro, E. A., Lee, C. M., Klymak, J. M., Molemaker, M. J., & McWilliams, J. C. (2013). Statistics of vertical vorticity, divergence, and strain in a developed submesoscale turbulence field. *Geophysical Research Letters*, *40*, 4706–4711. https://doi.org/10.1002/grl.50919

Siegelman, L. (2020). Energetic submesoscale dynamics in the ocean interior. *Journal of Physical Oceanography*, *50*(1), 727–749.

Siegelman, L., Klein, P., Rivière, P., Thompson, A. F., Torres, H. S., Flexas, M., & Menemenlis, D. (2020). Enhanced upward heat transport at deep submesoscale ocean fronts. *Nature Geoscience*, *13*, 50–55.

Small, R. J., Bryan, F. O., Bishop, S. P., & Tomas, R. A. (2019). Air-sea turbulent heat fluxes in climate models and observational analyses: What drives their variability? *Journal of Climate*, *32*(8), 2397–2421.

Su, Z., Wang, J., Klein, P., Thompson, A. F., & Menemenlis, D. (2018). Ocean submesoscales as a key component of the global heat budget. *Nature Communications*, *9*(1).

Tandon, A., & Garrett, C. (1994). Mixed layer restratification due to a horizontal density gradient. *Journal of Physical Oceanography*, *24*(6), 1419–1424.

Tandon, A., & Garrett, C. (1995). Geostrophic adjustment and restratification of a mixed layer with horizontal gradients above a stratified layer. *Journal of Physical Oceanography*, *25*(10), 2229–2241.

Taylor, S., & Straub, D. (2016). Forced near-inertial motion and dissipation of low-frequency kinetic energy in a wind-driven channel flow. *Journal of Physical Oceanography*, *46*(1), 79–93. https://doi.org/10.1175/JPO-D-15-0060.1

Thomas, L. N. (2017). On the modifications of near-inertial waves at fronts: Implications for energy transfer across scales. *Ocean Dynamics*, *67*(10), 1335–1350. https://doi.org/10.1007/s10236-017-1088-6

Thomas, L. N., Tandon, A., & Mahadevan, A. (2008). Submesoscale processes and dynamics. In *Ocean modeling in an eddying regime*, *Geophysical Monograph Series* (Vol. 177, pp. 17–38). Washington, D. C: American Geophysical Union.

Thompson, A. F., Lazar, A., Buckingham, C., Naveira Garabato, A. C., Damerell, G. M., & Heywood, K. J. (2016). Open-ocean submesoscale motions: A full seasonal cycle of mixed layer instabilities from gliders. *Journal of Physical Oceanography*, *46*(4), 1285–1307.

Torres, H. S., Klein, P., Menemenlis, D., Qiu, B., Su, Z., Wang, J., et al. (2018). Partitioning ocean motions into balanced motions and internal gravity waves: A modeling study in anticipation of future space missions. *Journal of Geophysical Research: Oceans*, *123*, 8084–8105. https://doi.org/10.1029/2018JC014438

Uchida, T., Abernathey, R., & Smith, S. (2017). Seasonality of eddy kinetic energy in an eddy permitting global climate model. *Ocean Modelling*, *118*, 41–58.

Viglione, G. A., Thompson, A. F., Flexas, M. M., Sprintall, J., & Swart, S. (2018). Abrupt transitions in submesoscale structure in Southern Drake Passage: Glider observations and model results. *Journal of Physical Oceanography*, *48*(9), 2011–2027. https://doi.org/10.1175/JPO-D-17-0192

Wolfe, C., Cessi, P., McClean, J., & Maltrud, M. (2008). Vertical heat transport in eddying ocean models. *Geophysical Research Letters*, *35*, L23605. https://doi.org/10.1029/2008GL036138

Xie, J. H., & Vanneste, J. (2015). A generalised-Lagrangian-mean model of the interactions between near-inertial waves and mean flow. *Journal of Fluid Mechanics*, *774*, 143–169.

Yang, H., Chang, P., Qiu, B., Zhang, Q., Wu, L., Chen, Z., & Wang, H. (2019). Mesoscale air-sea interaction and its role in eddy energy dissipation in the Kuroshio Extension. *Journal of Climate*, *32*(24), 8659–8676.

Yu, X., Naveira Garabato, A. C., Martin, A. P., Buckingham, C. E., Brannigan, L., & Su, Z. (2019). An annual cycle of submesoscale vertical flow and restratification in the upper ocean. *Journal of Physical Oceanography*, *49*(6), 1439–1461. https://doi.org/10.1175/JPO-D-18-0253.1